Enhanced soliton stability in bidirectionally coupled laser-microresonator systems

L. Bengel [1,*] H. Peng [2,*] B. de Rijk [1] C. Koos,[2] and W. Reichel [1,†]
[1]*Institute for Analysis (IANA), Karlsruhe Institute of Technology, 76131 Karlsruhe, Germany*
[2]*Institute of Photonics and Quantum Electronics (IPQ), Karlsruhe Institute of Technology, 76131 Karlsruhe, Germany*

(Received 24 April 2026; revised 13 July 2026; accepted 5 October 2026; published 3 November 2026)

We investigate a bidirectionally coupled system consisting of a Kerr-nonlinear microresonator and a continuous-wave single-mode semiconductor laser. Inside the resonator, a forward-propagating and a backscattered field interact nonlinearly, while a fraction of the backscattered field is fed back into the laser cavity. We demonstrate in this paper that the interaction of the laser with the feedback opens up new ways of stabilizing solitons. Using numerical bifurcation analysis, we systematically identify existence and stability ranges of time-harmonic soliton states in the anomalous dispersion regime. We show that, in contrast with the unidirectional configuration, the bidirectional coupling introduces a dynamic self-correcting response of the laser frequency that stabilizes solitons. We further corroborate these enhanced stability properties through Monte Carlo time integrations of randomly perturbed soliton states, demonstrating a significantly larger basin of attraction for solitons in the bidirectional system, consistent with existing experimental observations.

DOI: 10.1103/xw6j-58wy

I. INTRODUCTION

Chip-scale Kerr soliton comb generators using integrated optical microresonators have emerged as novel light sources that offer vast application potential. Providing tens or even hundreds of narrow-linewidth phase-locked tones with equidistant spacings of tens or hundreds of gigahertz (GHz), the devices are, e.g., particularly promising for massively parallel optical communications [1], low-noise microwave generation [2–5], or ultrabroadband photonic-electronic signal processing [6–9]. Recently, tremendous progress has been made regarding ultralow-loss optical waveguides, enabling Kerr-nonlinear microresonators with extremely high-Q factors of the order 10^7 or even 10^8 [10–12]. This results in milliwatt-level pump thresholds for Kerr comb generation [13], thereby allowing for pumping by III-V-based semiconductor laser diodes with moderate output power. A particularly promising approach to compact robust Kerr comb sources relies on directly coupling the pump laser diode to the Kerr-nonlinear microresonator without any intermediate optical isolator, leveraging resonantly enhanced backscattering from the cavity to precisely lock the laser emission wavelength to the pumped resonance [13–15].

This approach has been demonstrated both experimentally and theoretically to offer fully automatic soliton-comb formation by simply switching on the laser pump [13–17], thereby obviating complex electronic control systems and allowing for comb sources with a compact footprint that can be integrated into standard industrial packages. However, while a series of experimental demonstrations of self-injection-locked Kerr comb generators has been reported over the previous years [13–16], theoretical analysis and modeling of the full system have so far been limited to conventional time-integration techniques, which can describe the field evolution in specific comb-source implementations but cannot give a full picture of the stability and the properties of such comb states over a wider parameter range. Let us note that, in the regime of weak backscattering, bright and dark solitons have been investigated for a reduced model under the assumption of fast laser dynamics [18,19].

In this paper, we address this gap and develop a framework that allows us to investigate time-harmonic soliton states of the full bidirectionally coupled system using numerical bifurcation analysis in the anomalous dispersion regime. In contrast with time-integration methods, which were used in previous studies [13–15], our numerical bifurcation approach allows for a systematic exploration of soliton states for a large range of technically relevant parameter values. Our numerical analysis further shows that, unlike its unidirectionally coupled counterpart, the bidirectionally coupled laser-microresonator system can self-correct perturbations of the laser frequency such that stable time-harmonic solitons persist. To assess the robustness of these states, we perform Monte Carlo simulations of randomly perturbed soliton states, demonstrating that the bidirectional system possesses a substantially larger basin of attraction than the unidirectional configuration. Finally, we complement our study with a sensitivity analysis of the existence and stability ranges of soliton states with respect to key system parameters.

The paper is structured as follows. In Sec. II we formulate the mathematical model for the bidirectionally coupled

*These authors contributed equally to this work.
†Contact author: wolfgang.reichel@kit.edu

Published by the American Physical Society under the terms of the Creative Commons Attribution 4.0 International license. Further distribution of this work must maintain attribution to the author(s) and the published article's title, journal citation, and DOI.

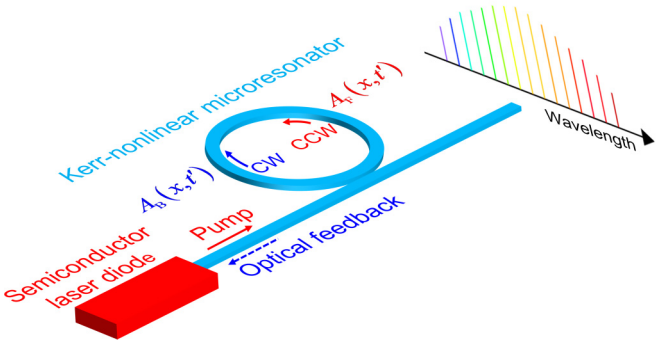


FIG. 1. Schematic diagram depicting the bidirectional coupling of the semiconductor laser with a Kerr microresonator. The light emitted from the semiconductor laser is injected into the Kerr microresonator in the CCW direction. Due to surface and internal inhomogeneities, the CCW field is backscattered CW and injected back into the semiconductor laser.

system. In Sec. III we present numerical simulations and compare our findings with those obtained in the standard unidirectionally coupled laser-microresonator model. In Appendix A we give details on the numerical bifurcation analysis as well as the algorithm for the parameter sensitivity analysis. Appendix B is devoted to the derivation of the normalized form of the bidirectionally coupled system from the system in physical quantities.

II. COUPLED LASER-RESONATOR MODEL EQUATIONS

Direct pumping of a Kerr-nonlinear microresonator with a semiconductor laser diode constitutes a bidirectionally coupled system, with resonantly enhanced Rayleigh backscattering within the microresonator feeding back into the laser cavity; see the conceptual diagram of the coupled system in Fig. 1. The light emitted from the pump laser is described by the carrier number $N(t')$ inside the cavity and the laser field $A_{\mathrm{L}}(t')$ which is coupled into the ring-shaped Kerr microresonator. A counterclockwise (CCW) propagating forward field $A_{\mathrm{F}}(x,t')$ and a clockwise (CW) propagating backscattered field $A_{\mathrm{B}}(x,t')$ are generated, where $x \in [0,2\pi]$ is the angular position and $t' \geqslant 0$ is the time. Inside the resonator, the fields A_{F} and A_{B} interact with each other, and a part of A_{B} is coupled out of the resonator back into the laser, where it interacts with the laser field A_{L}.

In the absence of backcoupling, the Kerr-nonlinear interaction in a high-Q microresonator pumped by a strong continuous-wave laser is described by the Lugiato-Lefever equation (LLE) [20,21]

$$\dot{a}_{\mathrm{F}}(x,t) = \left[-1 + \mathrm{i}d_2\frac{\partial^2}{\partial x^2} + \mathrm{i}|a_{\mathrm{F}}(x,t)|^2\right]a_{\mathrm{F}}(x,t) - \kappa_{\mathrm{ext}} f \mathrm{e}^{\mathrm{i}(\zeta t+\phi)} \tag{1}$$

in normalized time t and angular position $x \in [0,2\pi]$ (a superscripted dot denotes the time derivative). Here a_{F} is 2π periodic in x and describes the normalized forward-propagating optical field in the microresonator driven by the invariant laser field $a_{\mathrm{L}}(t) = f\mathrm{e}^{\mathrm{i}\zeta t}$ where the detuning $\zeta = \omega_{\mathrm{m}} - \omega_0$ is static and is given by the mismatch between the frequency ω_{m} of the pumped resonator mode and the frequency ω_0 of the laser cavity mode. Dispersion d_2, coupling κ_{ext}, and accumulative phase ϕ are as in Table I, and f represents the strength of the input laser.

TABLE I. Description of the physical meaning of the constants and their normalized counterparts. An empty space indicates that there is no normalized version of the corresponding quantity in the equations.

Quantity	Normalized quantity	Physical meaning
I/e	ι	Bias current of laser/elementary electronic charge
Γ	γ	Carrier recombination rate
N_0	n_0	Carrier number at transparency
μ		Optical mode confinement factor
α_{H}		Linewidth enhancement factor
K_{d}	κ_{d}	Photon decay rate of laser cavity
Ω_0	ω_0	Laser cavity mode frequency
K_{ext}	κ_{ext}	External coupling rate
K		Photon decay rate of resonator
Ω_{m}	ω_{m}	Frequency of resonator mode
D_2	d_2	Group-velocity dispersion
g_0		Single-photon-induced Kerr Frequency shift
K_{sc}	κ_{sc}	$\mathbb{C}$-valued coupling rate between forward and backward modes
ϕ		Accumulative phase between laser and resonator
σ		Small-signal gain
ϵ	ε	Saturation coefficient

The bidirectional setup considered in this paper is modeled by the system (2) below, which fundamentally differs from the LLE (1). First, the normalized carrier number n inside the laser is governed by a rate equation with a normalized gain factor $g = g(|a_{\mathrm{L}}|^2)$. This gain is subject to saturation by the laser field a_{L} and takes the explicit form

$$g(p) = \frac{\mu^2\sigma}{g_0 + \varepsilon p}, \quad p = |a_{\mathrm{L}}|^2.$$

See Table I for the physical meaning of the parameters. In addition, the equations for the normalized laser field a_{L}, the normalized forward field a_{F}, and the normalized backward field a_{B} are mutually coupled. Specifically, the laser field a_{L}, which is driven by the carriers, has the backscattered field a_{B} as an additional external injection source. Conversely, the forward field a_{F} is driven by the laser field a_{L}. Finally, inside the resonator the fields a_{F} and a_{B} are subject to self-phase modulation, dispersion, and cavity loss and interact through

center-mode coupling and cross-phase modulation. The resulting system for the normalized quantities, cf. [14,15], is given by

$$\begin{aligned}
\dot{n}(t) &= \iota - \gamma n(t) - g(|a_{\mathrm{L}}(t)|^2)[n(t)-1]|a_{\mathrm{L}}(t)|^2,\\
\dot{a}_{\mathrm{L}}(t) &= \left[\frac{1-\mathrm{i}\alpha_{\mathrm{H}}}{2}(g(|a_{\mathrm{L}}(t)|^2)n_0[n(t)-1]-\kappa_{\mathrm{d}})\right.\\
&\quad \left.+\,\mathrm{i}(\omega_{\mathrm{m}}-\omega_0)\right]a_{\mathrm{L}}(t)-\kappa_{\mathrm{ext}}a_{\mathrm{B}}(t)\mathrm{e}^{\mathrm{i}\phi},\\
\dot{a}_{\mathrm{F}}(x,t) &= \left[-1+\mathrm{i}d_2\frac{\partial^2}{\partial x^2}+\mathrm{i}[|a_{\mathrm{F}}(x,t)|^2+2|a_{\mathrm{B}}(t)|^2]\right]\\
&\quad \times a_{\mathrm{F}}(x,t)+\mathrm{i}\kappa_{\mathrm{sc}}a_{\mathrm{B}}(t)-\kappa_{\mathrm{ext}}a_{\mathrm{L}}(t)\mathrm{e}^{\mathrm{i}\phi},\\
\dot{a}_{\mathrm{B}}(t) &= \left[-1+\mathrm{i}\left(|a_{\mathrm{B}}(t)|^2+\frac{1}{\pi}\int_0^{2\pi}|a_{\mathrm{F}}(x,t)|^2\mathrm{d}x\right)\right]\\
&\quad \times a_{\mathrm{B}}(t)+\mathrm{i}\kappa_{\mathrm{sc}}^*\frac{1}{2\pi}\int_0^{2\pi}a_{\mathrm{F}}(x,t)\mathrm{d}x, \qquad (2)
\end{aligned}$$

where all constants are explained in Table I. The derivation of the system (2) for the normalized unknowns a_{F}, a_{L}, a_{B}, n from the associated system in the physical quantities A_{F}, A_{B}, A_{L}, N, is detailed in Appendix B.

While the forward field $a_{\mathrm{F}}(x,t)$ contains all resonator modes and therefore remains spatially dependent and 2π periodic in x, it suffices to only consider the central mode $a_{\mathrm{B}}(t)$ of the backscattered field, which is independent of x. The reason is as follows: for a laser pump modeled as a single-frequency laser diode, self-injection locking occurs only when the frequency detuning between the feedback injection field and the pump laser emission lies within the locking bandwidth [22]. Among all back-reflected modes, only the central mode, which originates from the back reflection of the pumped mode, has a frequency close to that of the pump-laser emission.

The unidirectional model (1) can be recovered from the bidirectional system (2) in the zero-backscattering limit. Specifically, by setting the coupling parameter κ_{sc} in (2) to zero, taking $a_{\mathrm{B}}(t)=0$, and choosing the injected laser field as $a_{\mathrm{L}}(t)=f\mathrm{e}^{\mathrm{i}\zeta t}$, the equation governing the forward field $a_{\mathrm{F}}(x,t)$ reduces to (1). Throughout this paper, we use this correspondence to perform direct quantitative comparisons between the two models, with all other parameters held fixed.

We remark that a reduced model of the laser-microresonator system, based on the assumptions of weak backscattering and fast laser dynamics, has also been considered in Refs. [18,19]. In the weak-backscattering regime, the direct influence of a_{B} on a_{F} is neglected, while its feedback to the laser is retained. Assuming that the laser amplitude relaxes rapidly, one sets $\frac{d}{dt}|a_{\mathrm{L}}|=0$. The laser frequency is then linked to the backscattered field through a laser phase equation, without explicitly evolving a_{L} and n as in (2). However, since the reduced model does not resolve how the laser field and carrier number respond in the stability analysis, we use system (2) to investigate the soliton robustness.

III. RESULTS AND COMPARISON BETWEEN UNIDIRECTIONALLY AND BIDIRECTIONALLY COUPLED SYSTEM

We present our results for the bidirectionally coupled system (2) and compare them with those of the unidirectional model (1). The physical parameter values used in our numerical simulations, together with their relation to the normalized parameters, are listed in Table II in Appendix B.

We begin by stating some known results for the standard LLE (1). It has been shown in Refs. [23–25] that it supports stable time-harmonic soliton solutions of the form $a_{\mathrm{F}}(x,t)=\underline{a}_{\mathrm{F}}^0(x)\mathrm{e}^{\mathrm{i}(\zeta t+\phi)}$ with $\zeta=\omega_{\mathrm{m}}-\omega_0$, which can be obtained via a bifurcation analysis. In this context, stability means that, while keeping the laser in its prescribed invariant state, small perturbations of the soliton solution in the microresonator's forward-propagating optical field a_{F} relax to a spatial translate of the solution on an exponentially fast timescale [26–29].

In contrast with conventional soliton generation in the unidirectional model (1) without backscattering, which typically requires a detuning sweep, the bidirectional system (2) enables turnkey formation of soliton states from small perturbations of the homogeneous zero state [13]. While this already demonstrates that backscattering can substantially facilitate soliton generation, our results show that the resulting time-harmonic soliton solutions of (2) also possess enhanced stability properties.

Before presenting our main results, we point out a key structural difference between the two models. The instantaneous laser frequency $\omega_{\mathrm{L}}(t)$ for system (2) is defined by

$$\omega_{\mathrm{L}}(t) := \omega_{\mathrm{m}} - \frac{\mathrm{d}}{\mathrm{d}t}\arg(a_{\mathrm{L}}(t)).$$

In the standard LLE model (1), the laser is prescribed, and its frequency is fixed by $\omega_{\mathrm{L}}(t)=\omega_0$. In the bidirectional model (2), by contrast, the laser field is affected by the resonator dynamics, so that $\omega_{\mathrm{L}}(t)$ is generally time-dependent and becomes part of the unknowns.

Our main results, demonstrating enhanced soliton stability in the bidirectional coupled system (2) compared with the unidirectional model (1), can now be summarized as follows:

(i) The bifurcation analysis, presented in Fig. 2, yields stable 2π periodic, time-harmonic soliton solutions to the bidirectional system (2) of the form

$$\begin{aligned}
a_{\mathrm{F}}(x,t) &= \underline{a}_{\mathrm{F}}^0(x)\mathrm{e}^{\mathrm{i}\zeta_{\mathrm{new}}t}, \qquad n(t)=n^0,\\
a_{\mathrm{L}}(t) &= \underline{a}_{\mathrm{L}}^0\mathrm{e}^{\mathrm{i}\zeta_{\mathrm{new}}t}, \qquad a_{\mathrm{B}}(t)=\underline{a}_{\mathrm{B}}^0\mathrm{e}^{\mathrm{i}\zeta_{\mathrm{new}}t}. \qquad (3)
\end{aligned}$$

They are qualitatively very similar to those found in the unidirectional model (1) while the laser is still operating in a continuous-wave mode with constant detuning $\zeta_{\mathrm{new}}=\omega_{\mathrm{m}}-\omega_{\mathrm{L}}=\zeta-\Delta\zeta$, where

$$\Delta\zeta = \frac{\kappa_{\mathrm{ext}}}{\underline{a}_{\mathrm{L}}^0}\,\mathrm{Im}\left[\underline{a}_{\mathrm{B}}^0\mathrm{e}^{\mathrm{i}\phi}(1+\mathrm{i}\alpha_{\mathrm{H}})\right],$$

and $\zeta=\omega_{\mathrm{m}}-\omega_0$. These solitons bifurcate from spatially constant, time-harmonic solutions to (2) of the form

$$\begin{aligned}
a_{\mathrm{F}}(t) &= \underline{a}_{\mathrm{F}}^{\mathrm{const}}\mathrm{e}^{\mathrm{i}\zeta_{\mathrm{new}}t}, \qquad n(t)=n^{\mathrm{const}},\\
a_{\mathrm{L}}(t) &= \underline{a}_{\mathrm{L}}^{\mathrm{const}}\mathrm{e}^{\mathrm{i}\zeta_{\mathrm{new}}t}, \quad a_{\mathrm{B}}(t)=\underline{a}_{\mathrm{B}}^{\mathrm{const}}\mathrm{e}^{\mathrm{i}\zeta_{\mathrm{new}}t}, \qquad (4)
\end{aligned}$$

with ζ as the bifurcation parameter.

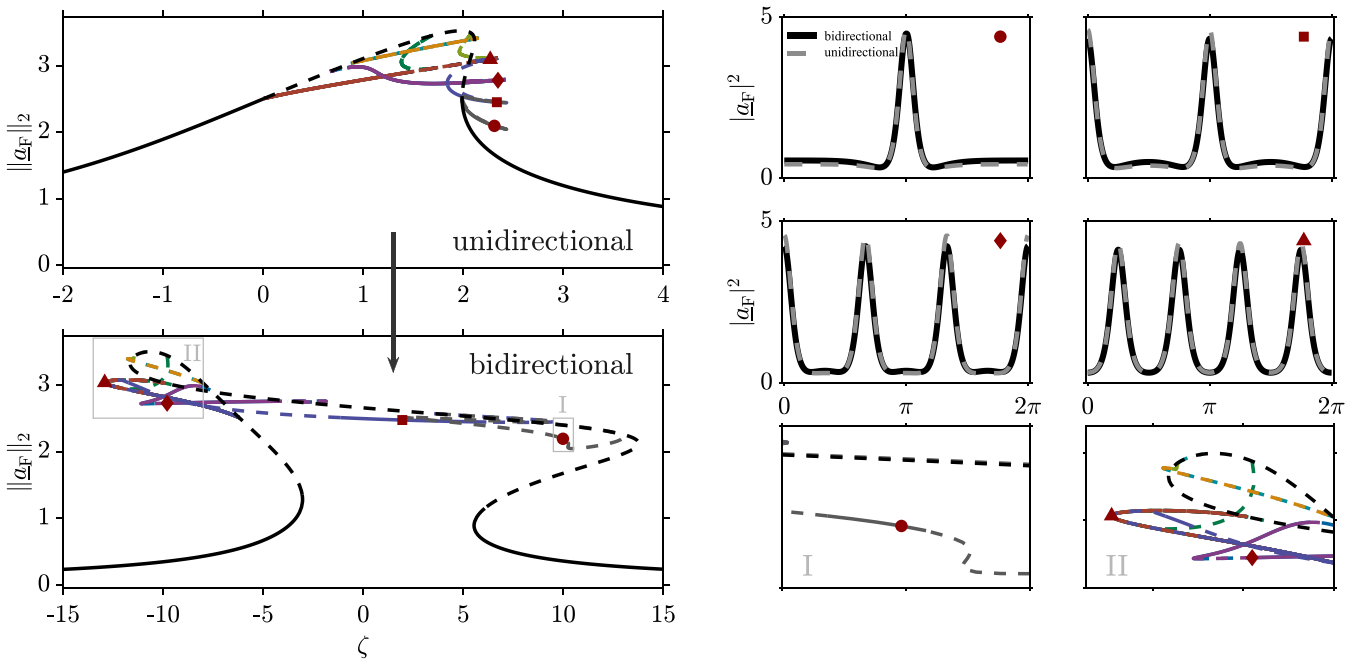


FIG. 2. The left column shows bifurcation diagrams of spatially 2π periodic, time-harmonic solutions of the form (3) in the unidirectional model (1) (top) and the bidirectionally coupled system (2) (bottom), with physical constants set as in Table II and $\phi = 0.64 \times \pi \approx 2.0106$, $\kappa_{\text{ext}} = 6.4550$. As a bifurcation parameter, we choose the frequency difference ζ. Stable (unstable) solutions are marked by a solid (dashed) line. The black curves indicate the spatially constant, time-harmonic solutions of the form (4), while different colors correspond to different bifurcating branches. For the bottom bifurcation diagram, we provide two enlargements for the regions I and II, which are displayed in the bottom row of the right column. Top rows of the right column show plots of the forward-field component $\underline{a}_F$ of solutions corresponding to one-, two-, three-, and four-soliton states, indicated in the bifurcation diagrams by the red dot, square, diamond, and triangle markers, respectively.

(ii) Applying perturbations to stable soliton solutions of the form (3), we find perturbed solutions $(n(t), a_L(t), a_F(x,t), a_B(t))$ to system (2) with the long-time asymptotics

$$\begin{aligned} n(t) &\to n^0, \\ a_L(t) &\to \underline{a}_L^0 e^{i(\zeta_{\text{new}} t + \phi_0)}, \\ a_F(x,t) &\to \underline{a}_F^0(x + x_0) e^{i(\zeta_{\text{new}} t + \phi_0)}, \\ a_B(t) &\to \underline{a}_B^0 e^{i(\zeta_{\text{new}} t + \phi_0)}, \\ \omega_L(t) &\to \omega_0 + \Delta\zeta, \end{aligned} \tag{5}$$

at an exponential rate as $t \to \infty$, see Fig. 3. Here, $\phi_0 = \int_0^\infty [\omega_L(s) - (\omega_0 + \Delta\zeta)]ds$ is a phase shift and x_0 is a translational displacement of the asymptotic steady state $\underline{a}_F^0$ induced by the perturbation. That is, in contrast with the unidirectional model (1) with a static laser field, backcoupling in the bidirectional system (2) causes the laser to automatically adjust and self-correct toward a time-harmonic continuous-wave mode with constant detuning.

(iii) The Monte Carlo simulations, presented in Fig. 4, demonstrate that the local basin of attraction of time-harmonic one-soliton solutions is significantly larger in the bidirectional system (2) than in the unidirectional model (1). Here, the local basin of attraction refers to the range of initial perturbation sizes for which perturbed solutions relax back to the (possibly shifted and rotated) one-soliton solution. This is reflected by a high convergence probability over a much larger range of perturbation sizes.

We next elaborate on points (i)–(iii), beginning with point (i), which concerns the numerical bifurcation analysis shown in Fig. 2. We computed bifurcation diagrams of spatially 2π-periodic, time-harmonic solutions of the form (3) for both the unidirectional model (1) and the bidirectional system (2). Along each branch, we numerically determined the stability of the corresponding solutions. The horizontal axis represents the detuning parameter ζ and the vertical axis displays the square root of the normalized intracavity pulse energy

$$\|\underline{a}_F\|_2 = \left(\int_0^{2\pi} |\underline{a}_F(x)|^2 dx \right)^{1/2}$$

of the forward-propagating optical field of the solution. In both bifurcation diagrams, we identified solutions corresponding to stable one-, two-, three-, and four-soliton states, indicated by a red dot, square, diamond, and triangle, respectively. Although the soliton states are qualitatively very similar in the two models, the overall bifurcation diagram and branch structure are noticeably deformed in the bidirectional case. Nevertheless, in both models the one-soliton states lie on the branch that emanates from the codimension-one bifurcation point (BP) encountered last when following the black solution curve, in agreement with the results for the unidirectional case [23]. In comparison with our investigation of the full bidirectional system (2), the recently published work of Ref. [19] on the reduced model in the weak backscat-

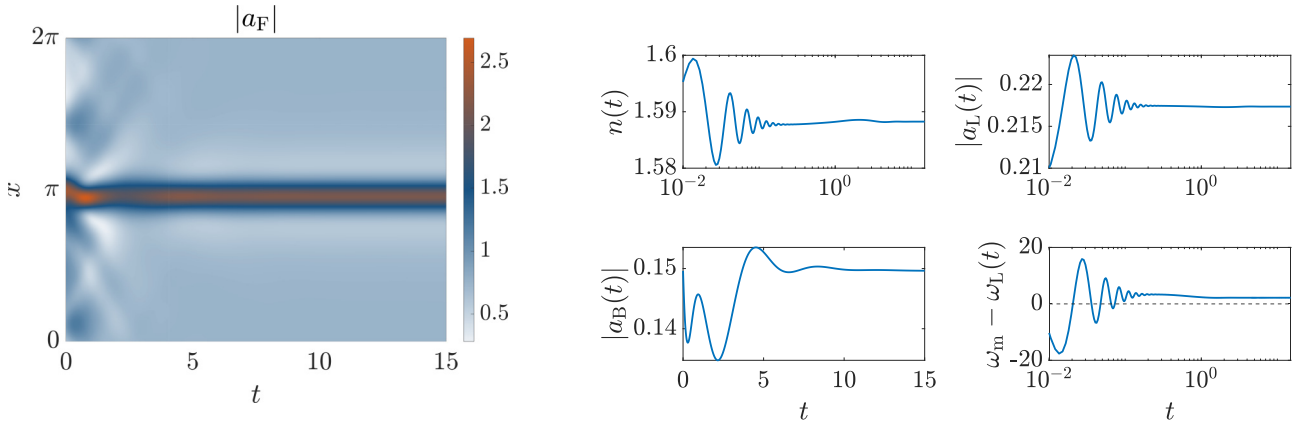


FIG. 3. Time integration for (2) starting from a small perturbation of the stable one-soliton solution marked with the red dot in Fig. 2. The left column shows a space-time plot of the forward field $a_F(x,t)$, where the color code indicates the magnitude $|a_F(x,t)|$. The right column shows simulations of the carrier number $n(t)$ (top left), magnitude of the laser field $|a_L(t)|$ (top right), the backward field $|a_B(t)|$ (bottom left), and the instantaneous laser frequency $\omega_m - \omega_L(t)$ (bottom right).

tering and fast laser dynamics regime also shows bifurcation of qualitatively similar pronounced single- and multisoliton stationary states. The approach of Refs. [18,19] of using the reduced model can be justified by looking at our time integration simulation of the full bidirectional model (2) in Fig. 3 and observing the almost two orders of magnitude faster relaxation times of the carrier numbers, the laser field, and the instantaneous laser frequency in comparison with the forward and backward field.

As described in (ii), the time-harmonic soliton states in the bidirectional system (2) have enhanced dynamical stability features as opposed to those in the unidirectional model (1). To illustrate these features, we use numerical time integration. We employ Lie-Trotter splitting with time steps of size 0.00015 and spatial grid size $\pi/2^8 \approx 0.012$ to approximate

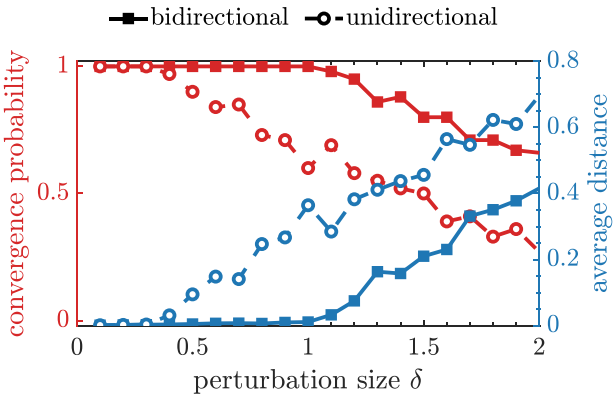


FIG. 4. Monte Carlo simulations assessing the stability of the time-harmonic one-soliton state marked by a red dot in Fig. 2. For each perturbation of $\|\cdot\|_2$-size δ, we perform 100 time integrations starting from the randomly perturbed one-soliton state. The figure shows the convergence probability to the soliton orbit and the average distance of the perturbed solution at time $t = 20$ from the one-soliton orbit, measured by $\||a_F(\cdot, t = 20)| - |\underline{a}_F^0|\|_2$. The results are shown for the bidirectionally coupled model and the unidirectional model.

the dynamics of the solution with the perturbed one-soliton state, which is marked by a red dot in Fig. 2 as the initial condition. The simulation in Fig. 3 confirms that a perturbation of the stable 1-soliton state causes all four unknowns to relax against a phase-rotated and translated version of the soliton as in (5). The translational shift x_0, whose value is fully determined by the initial perturbation, is visible in the left panel of Fig. 3. Moreover, the right panels show the long-term stabilization of the laser field's magnitude $|a_L(t)|$ and its instantaneous frequency $\omega_m - \omega_L(t)$. In particular, the frequency detuning is automatically adjusted to sustain a soliton solution. We emphasize that this self-correction of the laser found in the bidirectional system (2) cannot be observed in the unidirectional model (1) due to the static form of the laser field.

As outlined in (iii), we further assess the enhanced stability properties in the bidirectional model through Monte Carlo simulations, which provide a quantitative estimate of the local basin of attraction of time-harmonic one-soliton states. More precisely, we approximate the probability that an initially perturbed one-soliton state converges back to the soliton orbit, as the perturbation increases in size. Here, the soliton orbit is the family of solutions obtained from the soliton by arbitrary phase shifts and spatial translations. Figure 4 shows the result for the one-soliton displayed in Fig. 2 and marked by the red dot, both for the bidirectional system and the unidirectional model. For each data point, we perform 100 time integrations starting from randomly perturbed one-soliton states. The perturbations are applied to the forward field and are taken to be of the form $a_F^{\text{pert}}(x) = \sum_{k=0}^{4} \alpha_k \cos(kx)$, where the randomly chosen coefficients α_k are normalized such that $\|a_F^{\text{pert}}\|_2 = \delta$. This choice ensures that the perturbations are smooth and that the resulting solutions remain even. Therefore, it is sufficient to measure the distance to the orbit generated by phase rotations. We perturb only the a_F-field in order to obtain a quantitative comparison with the unidirectional model. At time $t = 20$, we measure the distance between the perturbed solution a_F and the one-soliton orbit by $\||a_F(\cdot, t = 20)| - |\underline{a}_F^0|\|_2$. If this distance is smaller than the prescribed threshold

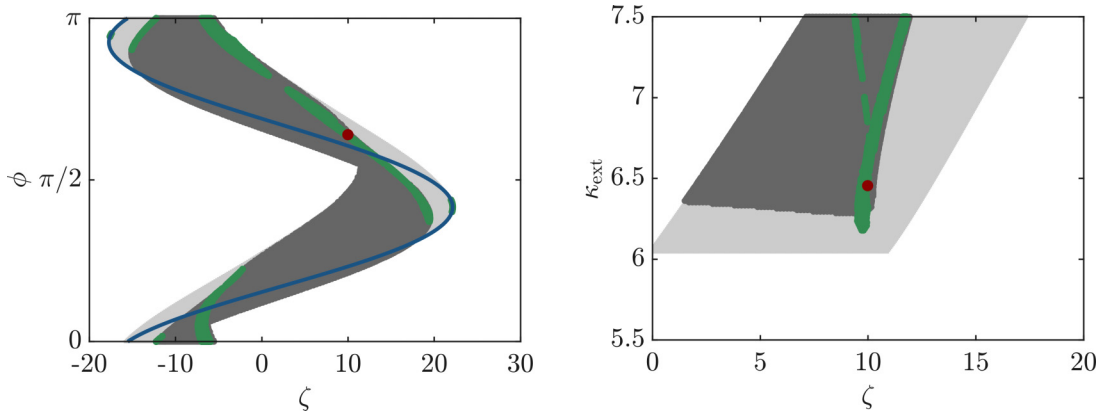


FIG. 5. Existence and stability regions in the ζ–ϕ plane (left) and ζ–κ_{ext} plane (right) of spatially 2π-periodic, time-harmonic one-soliton solutions to (2) of the form (3), bifurcating from spatially constant, time-harmonic solutions of the form (4). The light-gray area shows the one-soliton existence range, and the dark-gray subsets depict the range of one-solitons with FWHMs of at most 0.4. The green subset indicates stable solutions. The red dot marks the position of the one-soliton state of Fig. 2. The blue curve in the left panel indicates the position of the BP from which the one-solitons emerge. The parameters are fixed to the physical values in Table II, with $\kappa_{\text{ext}} = 6.455$ in the left panel and $\phi = 0.64 \times \pi$ in the right panel.

0.5, the simulation is classified as convergent. Figure 4 shows that, for the bidirectionally coupled model, convergence occurs with probability nearly one up to $\delta = 1$. In contrast, for the unidirectional model, this threshold is already reached at $\delta = 0.3$. In addition, Figure 4 shows that the average distance of the perturbed solution to the soliton orbit at $t = 20$ is much smaller in the bidirectional model for increasing values of δ. All in all, this demonstrates that the bidirectional coupling significantly increases the local basin of attraction of one-soliton states compared with the standard LLE.

Next, we systematically analyze the influence of the parameters ϕ and κ_{ext} on the existence and stability ranges of time-harmonic one-soliton solutions to the bidirectional system (2). This is of particular interest for practical applications as both parameters can be changed in the experimental setup [13,14,30]. The sensitivity analysis relies on an Algorithm 1 based on numerical path continuation. The Algorithm 1 is explained in detail in Appendix A, and here we only outline its main steps. First, we compute the curve of spatially constant, time-harmonic solutions of the form (4) and determine all BPs from which one-soliton solutions of the form (3) can emerge. We then perform continuation in the parameter ζ starting from the BPs as long as the solutions on the bifurcating branches retain the shape of a single pulse. Stability of the solutions is checked by computing the eigenvalues of the Jacobian evaluated at the respective states. The results are shown in Fig. 5. Here, each point in the light gray regions represents a pair (ζ, ϕ) (left panel) or $(\zeta, \kappa_{\text{ext}})$ (right panel) for which a one-soliton solution can be found. The dark gray regions indicate subsets of the existence range that consist of highly localized one-solitons with a prescribed full width at half maximum (FWHM) value of at most 0.4, and stable solutions are indicated by a green color. In addition, the blue line in the left panel shows the values of the parameters at which these solitons bifurcate from the spatially constant, time-harmonic states. Finally, we have included red dots in both charts to indicate the position of the stable one-soliton from Fig. 2.

For the accumulated phase ϕ, we observe that the existence and stability ranges bend from negative values of ζ to positive values, and then back to negative, as ϕ increases from 0 to π. We note that, due to the symmetry

$$(\underline{a}_{\text{F}}, \underline{a}_{\text{B}}, \underline{a}_{\text{L}}, n, \phi) \mapsto (\underline{a}_{\text{F}}, \underline{a}_{\text{B}}, -\underline{a}_{\text{L}}, n, \phi + \pi)$$

of (2), the existence and stability ranges are π periodic in ϕ and thus we can deduce from Fig. 5 the existence and stability ranges for all values of $\phi \in [0, 2\pi]$. The simulations show that stable solutions can be found near the boundaries of the dark-gray areas, which represent highly localized soliton states. Moreover, we observe gaps in the stability regions for certain values of ϕ. This indicates that the accumulated phase needs to be carefully tuned in order to support stable one-soliton states.

The right panel of Fig. 5 depicts the sensitivity with respect to the coupling κ_{ext}, where the remaining parameters are fixed to the physical values in Table II. We observe that bifurcating branches supporting one-soliton solutions emerge only when κ_{ext} exceeds approximately 6.0. As κ_{ext} is further increased, we find highly localized soliton solutions with a FWHM of at most 0.4. This is explained by the fact that low values of κ_{ext} lead to a small excitation of the cavity field, obstructing the existence of localized states, whereas high values allow for energy transfer from the laser to the microresonator, resulting in strong forcing. As in the sensitivity study with respect to ϕ, large parts of the stability range for one-solitons lie close to the boundary of the dark-gray region of highly localized states. Finally, when κ_{ext} exceeds approximately 6.8, a second disconnected stability region emerges.

IV. SUMMARY

We have investigated the bidirectionally coupled system (2) of a continuous-wave laser and a Kerr-nonlinear microresonator, where the backward-propagating resonator field interacts with the pump laser. Using numerical bifurcation tools, we have shown that the system supports stable time-harmonic soliton states with stationary instantaneous laser frequency $\omega_{\text{L}} = \omega_0 + \Delta\zeta$. Under sufficiently small initial perturbations of these states, we demonstrated that not only the laser and microresonator fields relax toward the solitons, but, most importantly, $\omega_{\text{L}}(t)$ self-corrects toward the value

$\omega_0 + \Delta\zeta$ which sustains the soliton state. Such a dynamic self-correction of the laser is impossible for the standard LLE where the laser field has a static frequency. Utilizing Monte Carlo simulations, we further showed that bidirectional laser-resonator coupling enlarges the basin of attraction for one-soliton states compared with the unidirectional model, providing a route toward enhancing soliton stability in experiments. Finally, we systematically explored existence and stability ranges of solitons with respect to parameter variations of the accumulated phase ϕ and the external coupling strength κ_{ext}. It turns out that stable one-solitons can only exist provided ϕ lies within a finite band of values and the external coupling strength κ_{ext} exceeds a minimal value.

ACKNOWLEDGMENTS

This project is funded by the Deutsche Forschungsgemeinschaft (DFG, German Research Foundation)–Project-ID 258734477–SFB 1173. The authors thank Tobias Jahnke (KIT) for providing the MATLAB code used for the time-integration simulations. Moreover, the authors thank the anonymous reviewers for their valuable comments, which substantially improved this paper.

DATA AVAILABILITY

The data that support the findings of this article are openly available [31].

APPENDIX A: NUMERICAL BIFURCATION AND SENSITIVITY ANALYSIS

Here we explain the setup of the numerical bifurcation analysis, and we introduce the Algorithm 1 which we use for analyzing the sensitivity of the one-soliton existence range with respect to parameter variations.

First, note that, if the unknowns a_{L}, a_{F}, and a_{B} in (2) are all shifted by a common constant phase factor, then they still solve the same system. This means that, in contrast with the standard Lugiato-Lefever equation (1), which is only invariant under spatial shifts, the system (2) has an additional invariance under phase shifts of a_{L}, a_{F}, a_{B}. We eliminate the phase invariance by transitioning into a rotating frame in which the laser field a_{L} is real-valued. This is necessary for a robust convergence of the numerical bifurcation algorithm since in this way we exclude continuation of nontrivial states in the direction where all components are shifted by a constant phase factor. To this end, we write the laser field in polar coordinates

$$a_{\text{L}}(t) = r(t)\mathrm{e}^{-\mathrm{i}\int_0^t(\omega_{\text{L}}(s)-\omega_{\text{m}})\mathrm{d}s}, \quad r(t) = |a_{\text{L}}(t)|,$$

where we recall that $\omega_{\text{L}}(t) - \omega_{\text{m}} = -\frac{d}{dt}\arg(a_{\text{L}}(t))$. Moreover, we introduce $\underline{a}_{\text{F}}, \underline{a}_{\text{B}}$ defined by

$$a_{\text{F}}(x,t) = \underline{a}_{\text{F}}(x,t)\mathrm{e}^{-\mathrm{i}\int_0^t(\omega_{\text{L}}(s)-\omega_{\text{m}})\mathrm{d}s},$$
$$a_{\text{B}}(t) = \underline{a}_{\text{B}}(t)\mathrm{e}^{-\mathrm{i}\int_0^t(\omega_{\text{L}}(s)-\omega_{\text{m}})\mathrm{d}s}.$$

Substituting the formula for a_{L} into (2), we obtain an equation for the instantaneous laser frequency

$$\omega_{\text{L}}(t) = \omega_0 + \tfrac{1}{2}\alpha_{\text{H}}\{g(r(t)^2)n_0[n(t)-1] - \kappa_{\text{d}}\} + \frac{\kappa_{\text{ext}}}{r(t)}\,\mathrm{Im}[\underline{a}_{\text{B}}(t)\mathrm{e}^{\mathrm{i}\phi}]. \tag{A1}$$

With the shorthand

$$\Theta(r,z,n) := \frac{1}{2}\alpha_{\text{H}}[g(r^2)n_0(n-1) - \kappa_{\text{d}}] + \frac{\kappa_{\text{ext}}}{r}\,\mathrm{Im}\left(z\mathrm{e}^{\mathrm{i}\phi}\right)$$

and the frequency offset $\zeta = \omega_{\text{m}} - \omega_0$, the remaining system for n, r, $\underline{a}_{\text{F}}$, $\underline{a}_{\text{B}}$ becomes (we suppress their arguments)

$$\begin{aligned}
\dot{n} &= \iota - \gamma n - g(r^2)(n-1)r^2,\\
\dot{r} &= \frac{1}{2}[g(r^2)n_0(n-1) - \kappa_{\text{d}}]r - \kappa_{\text{ext}}\,\mathrm{Re}\left(\underline{a}_{\text{B}}\mathrm{e}^{\mathrm{i}\phi}\right),\\
\dot{\underline{a}}_{\text{F}} &= [-1 - \mathrm{i}[\zeta - \Theta(r,\underline{a}_{\text{B}},n)] + \mathrm{i}d_2\frac{\partial^2}{\partial x^2}\\
&\quad + \mathrm{i}(|\underline{a}_{\text{F}}|^2 + 2|\underline{a}_{\text{B}}|^2)]\underline{a}_{\text{F}} + \mathrm{i}\kappa_{\text{sc}}\underline{a}_{\text{B}} - \kappa_{\text{ext}}r\mathrm{e}^{\mathrm{i}\phi},\\
\dot{\underline{a}}_{\text{B}} &= \Bigg[\left[-1 - \mathrm{i}(\zeta - \Theta(r,\underline{a}_{\text{B}},n)\right]\\
&\quad + \mathrm{i}\left(|\underline{a}_{\text{B}}|^2 + \frac{2}{2\pi}\int_0^{2\pi}|\underline{a}_{\text{F}}(x,\cdot)|^2\mathrm{d}x\right)\Bigg]a_{\text{B}}\\
&\quad + \mathrm{i}\kappa_{\text{sc}}^*\frac{1}{2\pi}\int_0^{2\pi}\underline{a}_{\text{F}}(x,\cdot)\mathrm{d}x.
\end{aligned} \tag{A2}$$

Observe that in this system the invariance under phase-shifts is no longer present since r is a real-valued quantity.

When searching for steady states of (A2), we set the time derivatives $\dot{n}$, $\dot{r}$, $\dot{\underline{a}}_{\text{F}}$, $\dot{\underline{a}}_{\text{B}}$ to zero. This results in an ordinary differential equation (ODE) for $\underline{a}_{\text{F}}$ coupled to three algebraic equations for the remaining fields which include nonlocal terms of $\underline{a}_{\text{F}}$. For the instantaneous laser frequency ω_{L}, Eq. (A1) implies that it will also be constant. This means that stationary solutions of (A2) correspond to time-harmonic solutions of (2). Combing (A1) and the equation for r in (A2) we obtain

$$\omega_{\text{L}} = \omega_0 + \frac{\kappa_{\text{ext}}}{r}\,\mathrm{Im}[\underline{a}_{\text{B}}\mathrm{e}^{\mathrm{i}\phi}(1+\mathrm{i}\alpha_{\text{H}})].$$

The steady-state equation for n can be solved in terms of r, yielding the formula

$$n = n(r) = \frac{\iota + g(r^2)r^2}{\gamma + g(r^2)r^2}.$$

Upon substituting this into the system (A2), we obtain an ODE for $\underline{a}_{\text{F}}$, coupled to two algebraic equations for r and $\underline{a}_{\text{B}}$, given by

$$\begin{aligned}
0 &= \Bigg[-1 - \mathrm{i}[\zeta - \Theta(r,\underline{a}_{\text{B}},n(r))] + \mathrm{i}d_2\frac{\partial^2}{\partial x^2}\\
&\quad + \mathrm{i}(|\underline{a}_{\text{F}}|^2 + 2|\underline{a}_{\text{B}}|^2)\Bigg]\underline{a}_{\text{F}} + \mathrm{i}\kappa_{\text{sc}}\underline{a}_{\text{B}} - \kappa_{\text{ext}}r\mathrm{e}^{\mathrm{i}\phi},\\
0 &= \frac{1}{2}\{g(r^2)n_0[n(r)-1] - \kappa_{\text{d}}\}r - \kappa_{\text{ext}}\,\mathrm{Re}\left(\underline{a}_{\text{B}}\mathrm{e}^{\mathrm{i}\phi}\right),\\
0 &= \Bigg[-1 - \mathrm{i}[\zeta - \Theta(r,\underline{a}_{\text{B}},n(r))]\\
&\quad + \mathrm{i}\left(|\underline{a}_{\text{B}}|^2 + \frac{2}{2\pi}\int_0^{2\pi}|\underline{a}_{\text{F}}(x)|^2\mathrm{d}x\right)\Bigg]\underline{a}_{\text{B}}\\
&\quad + \mathrm{i}\kappa_{\text{sc}}^*\frac{1}{2\pi}\int_0^{2\pi}\underline{a}_{\text{F}}(x)\mathrm{d}x.
\end{aligned} \tag{A3}$$

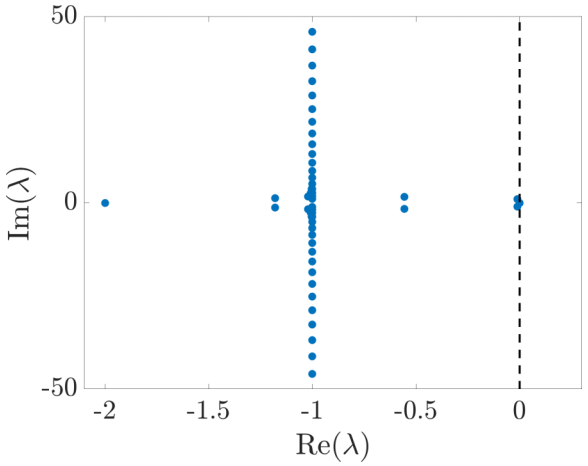


FIG. 6. Eigenvalues of the Jacobian operator evaluated at the one-soliton state in Fig. 2 (red dot) of the bidirectional model. We see that all eigenvalues except for the zero eigenvalue have strictly negative real part, indicating dynamical stability and relaxation to a spatial translation of the one-soliton solution at an exponential rate.

We consider the ODE for $\underline{a}_{\mathrm{F}}$ on the interval $x \in [0, \pi]$ equipped with homogeneous Neumann boundary conditions

$$\partial_x \underline{a}_{\mathrm{F}}(0) = \partial_x \underline{a}_{\mathrm{F}}(\pi) = 0. \tag{A4}$$

This eliminates the spatial shift invariance of $\underline{a}_{\mathrm{F}}$ in (A2), which is necessary to avoid unwanted path continuation in the translational direction. Note that we recover periodic solutions on $[0, 2\pi]$ by reflection:

$$\underline{a}_{\mathrm{F,per}}(x) = \begin{cases} \underline{a}_{\mathrm{F}}(x), & x \in [0, \pi] \\ \underline{a}_{\mathrm{F}}(2\pi - x), & x \in [\pi, 2\pi]. \end{cases}$$

We then perform the numerical bifurcation analysis for (A3) and (A4). The bifurcation analysis is conducted using the MATLAB package PDE2PATH [32], which is designed for the numerical continuation and bifurcation analysis of systems of partial differential equations (PDEs). We discretize the boundary-value problem for $\underline{a}_{\mathrm{F}}$ using linear finite elements, and add the equations for $\underline{a}_{\mathrm{B}}$ and r as algebraic constraints. Throughout our bifurcation experiments, we choose the frequency offset ζ as the bifurcation parameter, since it can be varied in the physical experiments.

Stability of the bifurcating solutions can be determined by computing the eigenvalues of the Jacobian $\mathcal{J}$ associated with the discretized version of (A3). For this purpose it is necessary to reintroduce the translational invariance by using periodic boundary conditions on $[0, 2\pi]$ for the field $\underline{a}_{\mathrm{F}}$ as otherwise only stability with respect to even perturbations is determined. Thus, the solution is stable if all eigenvalues λ of $\mathcal{J}$ satisfy $\mathrm{Re}(\lambda) < 0$ with the exception of a zero eigenvalue present due to the continuous shift symmetry of the system. As a result, stable solutions exhibit a spectral gap (if we neglect the zero eigenvalue), which causes a relaxation of the perturbed solutions to a spatial translate of it on exponentially fast timescales, cf. Fig. 3. Figure 6 shows the stable spectrum of the one-soliton in the bidirectional system obtained in Fig. 2 and marked by the red dot.

ALGORITHM 1. For $j = 1, \ldots, m$ do.

1. Set $\varsigma = \varsigma_j$ and compute the constant solution curve with bifurcation parameter $\zeta \in [\zeta_{\min}, \zeta_{\max}]$.
2. Mark all nondegenerate BPs on this curve for which (A5) holds with $k = 1$.
3. Compute and plot all bifurcation branches starting from the marked BPs of Step 2 in ζ as long as the forward-field component $\underline{a}_{\mathrm{F}}$ satisfies the following conditions:
   (i) $\{x_{\max}\} = \arg\max_x |\underline{a}_{\mathrm{F}}(x)|^2 \subset \{0, \pi\}$,
   (ii) $\left| \frac{\int_{\pi/2}^{x_{\max}} |\underline{a}_{\mathrm{F}}'(z)|^2 \mathrm{d}z}{\int_{\pi/2}^{\pi - x_{\max}} |\underline{a}_{\mathrm{F}}'(z)|^2 \mathrm{d}z} \right| > 1.75.$

The bifurcation analysis is also used to algorithmically determine (a subset of) the one-soliton existence range in the parameter space. To describe our algorithm for the sensitivity analysis, we need an auxiliary result from bifurcation theory. Suppose that $(\underline{a}_{\mathrm{F},0}, r, \underline{a}_{\mathrm{B},0}, \zeta_0) \in \mathbb{C} \times \mathbb{R} \times \mathbb{C} \times \mathbb{R}$ is a nondegenerate BP on the constant solution curve, where nondegenerate means that zero is a simple eigenvalue of the associated Jacobian of (A3). Then the forward-field component of the bifurcating solutions can be locally parametrized by $s \in (-s_0, s_0)$ with some $0 < s_0 \ll 1$ [33, Corollary I.4.2]. More precisely, we have the expansion

$$\underline{a}_{\mathrm{F}}(x; s) = \underline{a}_{\mathrm{F},0} + \underline{a}_{\mathrm{F},1} \cos(kx)s + O(s^2) \text{ as } s \to 0, \tag{A5}$$

with $k \in \mathbb{N}_0$ and $\underline{a}_{\mathrm{F},1} \in \mathbb{C}$. Below, we use this formula for $k = 1$ to determine those BPs at which one-solitons branch away from flat states. Now let us fix a system parameter ς different from ζ. We analyze the influence of ς on the existence range of the one-solitons. Therefore, we chose a discretization $\varsigma_{\min} = \varsigma_1 < \varsigma_2 < \cdots < \varsigma_m = \varsigma_{\max}$ with $m \in \mathbb{N}$. Our algorithm consists of three steps given in Algorithm 1.

We briefly comment on each step. Steps 1 and 2 are necessary to compute nontrivial solutions of (A3), where Step 2 ensures that we only calculate bifurcation branches on which we expect to find one-soliton states. Heuristically, we have observed that k_0-solitons emerge from BPs where (A5) holds with $k = k_0$. This observation is consistent with simulations in Ref. [23] for the standard LLE (1). Once we are on a one-soliton branch, we stop the continuation as soon as the solutions deform into two-soliton states (or different wave forms). In system (A3) we observed that a one-soliton branch generically connects to a two-soliton branch. The stopping criteria are given by conditions (i) and (ii) in Step 3. The first ensures that the modulus squared of the periodic extension of $\underline{a}_{\mathrm{F}}(x)$ has a single maximum on the periodicity cell $[0, 2\pi]$, while the second ensures that the solutions are sufficiently localized around this maximum. Note that the value 1.75 determines the degree of localization; it can also be varied, with low values meaning that we look for a low degree of localization, while high values enforce a high degree of localization.

APPENDIX B: DERIVATION OF THE NORMALIZED SYSTEM FROM THE PHYSICAL MODEL

Here we show how the normalized coupled system (2) is derived from the system in physical units, and we give the

values of the physical and normalized parameters used in our simulations.

The bidirectionally coupled laser-resonator system in physical units is given by [14,15]

$$\begin{aligned}
\dot{N}(t') &= \frac{I}{e} - \Gamma N(t') - \frac{\mu^2\sigma}{1+\epsilon|A_{\rm L}(t')|^2}[N(t')-N_0]|A_{\rm L}(t')|^2,\\
\dot{A}_{\rm L}(t') &= \left[\frac{1-{\rm i}\alpha_{\rm H}}{2}\left(\frac{\mu^2\sigma}{1+\epsilon|A_{\rm L}(t')|^2}[N(t')-N_0]-K_{\rm d}\right)\right.\\
&\quad \left.+{\rm i}(\Omega_{\rm m}-\Omega_0)\right]A_{\rm L}(t') - K_{\rm ext}A_{\rm B}(t'){\rm e}^{{\rm i}\phi},\\
\dot{A}_{\rm F}(x,t') &= \left[-\frac{K}{2}+{\rm i}D_2\frac{\partial^2}{\partial x^2}+{\rm i}g_0[|A_{\rm F}(x,t')|^2+2|A_{\rm B}(t')|^2]\right]\\
&\quad \times A_{\rm F}(x,t')+{\rm i}K_{\rm sc}A_{\rm B}(t')-K_{\rm ext}A_{\rm L}(t'){\rm e}^{{\rm i}\phi},\\
\dot{A}_{\rm B}(t') &= \left[-\frac{K}{2}+{\rm i}g_0\left(|A_{\rm B}(t')|^2+\frac{1}{\pi}\int_0^{2\pi}|A_{\rm F}(x,t')|^2{\rm d}x\right)\right]\\
&\quad \times A_{\rm B}(t')+{\rm i}K_{\rm sc}^*\frac{1}{2\pi}\int_0^{2\pi}A_{\rm F}(x,t'){\rm d}x. \qquad \text{(B1)}
\end{aligned}$$

The physical meaning of the constants are explained in Table I and the normalized constants are given by

$$\begin{aligned}
&\iota = 2\frac{I}{KN_0e}, \quad \gamma = 2\frac{\Gamma}{K}, \quad \kappa_{\rm d} = 2\frac{K_{\rm d}}{K},\\
&\omega_{\rm m} = 2\frac{\Omega_{\rm m}}{K}, \quad \omega_0 = 2\frac{\Omega_0}{K}, \quad \kappa_{\rm ext} = 2\frac{K_{\rm ext}}{K}, \quad d_2 = 2\frac{D_2}{K},\\
&\kappa_{\rm sc} = 2\frac{K_{\rm sc}}{K}, \quad n_0 = 2g_0\frac{N_0}{K}, \quad \varepsilon = \frac{\epsilon K}{2}.
\end{aligned}$$

TABLE II. Values of the physical constants and their normalized counterparts. An empty space indicates that there is no normalized version of the corresponding quantity in the equations. Since our simulations focus on laser dynamics induced by external optical feedback rather than high-power or large-signal modulation effects, we assume that the laser operates in the linear gain regime, with its output power remaining well below the saturation power. Accordingly, the gain compression effect is neglected by setting the gain saturation coefficient $\varepsilon = 0$.

Quantity	Value	Normalized quantity	Value
I/e	$\frac{0.5359}{1.6\times10^{-19}}$ A/C	ι	41.4466
Γ	1×10^9 s^{-1}	γ	2.6526
N_0	2.1436×10^8	n_0	1.0610
μ	0.5		
$\alpha_{\rm H}$	2.5		
$K_{\rm d}$	$5\times10^{10}\times2\pi$ rad/s	$\kappa_{\rm d}$	833.3333
$K_{\rm ext}$	$[5.5, 7.5]\times120\times10^6\times\pi$ rad/s	$\kappa_{\rm ext}$	[5.5,7.5]
K	$120\times10^6\times2\pi$ rad/s		
D_2	$7.5\times10^6\times2\pi$ rad/s	d_2	0.125
g_0	1.866 rad/s		
$K_{\rm sc}$	$15\times10^6\times2\pi$ rad/s	$\kappa_{\rm sc}$	0.25
ϕ	$[0,\pi]$		
σ	1×10^4 s^{-1}		
ϵ	0	ε	0

The system (2) is then obtained by the transformation

$$\begin{aligned}
&a_{\rm F}(x,t) = \sqrt{\frac{2g_0}{K}}A_{\rm F}(x,t'), \quad a_{\rm B}(t) = \sqrt{\frac{2g_0}{K}}A_{\rm B}(t'),\\
&a_{\rm L}(t) = \sqrt{\frac{2g_0}{K}}A_{\rm L}(t'), \quad n(t) = N_0^{-1}N(t'), \quad t' = \frac{2}{K}t.
\end{aligned}$$

[1] P. Marin-Palomo, J. N. Kemal, T. J. Kippenberg, W. Freude, S. Randel, and C. Koos, Performance of chip-scale optical frequency comb generators in coherent WDM communications, Opt. Express **28**, 12897 (2020).

[2] Q.-X. Ji, W. Zhang, A. Savchenkov, P. Liu, S. Sun, W. Jin, J. Guo, J. Peters, L. Wu, A. Feshali, M. Paniccia, V. Ilchenko, J. Bowers, A. Matsko, and K. Vahala, Dispersive-wave-agile optical frequency division, Nat. Photon. **19**, 624 (2025).

[3] X. Jin, Z. Xie, X. Zhang, H. Hou, B. Wu, F. Zhang, X. Zhang, L. Chang, Q. Gong, and Q.-F. Yang, Microresonator-referenced soliton microcombs with zeptosecond-level timing noise, Nat. Photon. **19**, 630 (2025).

[4] S. Sun, B. Wang, K. Liu, M. W. Harrington, F. Tabatabaei, R. Liu, J. Wang, S. Hanifi, J. S. Morgan, M. Jahanbozorgi, Z. Yang, S. M. Bowers, P. A. Morton, K. D. Nelson, A. Beling, D. J. Blumenthal, and X. Yi, Integrated optical frequency division for microwave and mmWave generation, Nature (London) **627**, 540 (2024).

[5] Y. Zhao, J. K. Jang, G. J. Beals, K. J. McNulty, X. Ji, Y. Okawachi, M. Lipson, and A. L. Gaeta, All-optical frequency division on-chip using a single laser, Nature (London) **627**, 546 (2024).

[6] D. Drayss, D. Fang, C. Füllner, G. Lihachev, T. Henauer, Y. Chen, H. Peng, P. Marin-Palomo, T. Zwick, W. Freude, T. J. Kippenberg, S. Randel, and C. Koos, Non-sliced optical arbitrary waveform measurement (OAWM) using soliton microcombs, Optica **10**, 888 (2023).

[7] D. Fang, D. Drayss, H. Peng, G. Lihachev, C. Füllner, A. Kuzmin, P. Marin-Palomo, P. Matalla, P. Kharel, R. N. Wang, J. Riemensberger, M. Zhang, J. Witzens, J. C. Scheytt, W. Freude, S. Randel, T. J. Kippenberg, and C. Koos, 320 GHz photonic-electronic analogue-to-digital converter (ADC) exploiting Kerr soliton microcombs, Light: Sci. Appl. **14**, 241 (2025).

[8] H. Peng, Y. Chen, D. Fang, C. Bremauer, G. Lihachev, D. Drayss, J. Riemensberger, A. Sherifaj, M. Lu, A. Voloshin, S. T. Skacel, M. Lauermann, T. Zwick, W. Freude, S. Randel, T. J. Kippenberg, and C. Koos, Optical arbitrary waveform generation (OAWG) using self-injection-locked RF-synchronized Kerr soliton microcombs, in *CLEO 2025*, Technical Digest

Series (Optica Publishing Group, Washington, DC, 2025), paper SS164_1.

[9] H. Peng, L. Schmitz, D. Drayss, Y. Zheng, V. Lauinger, B. Geiger, Y. Xu, D. Fang, W. Freude, S. Randel, K. Yvind, L. Schmalen, M. Pu, and C. Koos, 400 GBd 32QAM transmission using RF-synchronized dark-soliton microcombs for optical arbitrary waveform generation (OAWG), in *2025 European Conference on Optical Communications (ECOC)* (IEEE, Piscataway, NJ, 2025), pp. 1–4.

[10] J. Liu, G. Huang, R. N. Wang, J. He, A. S. Raja, T. Liu, N. J. Engelsen, and T. J. Kippenberg, High-yield, wafer-scale fabrication of ultralow-loss, dispersion-engineered silicon nitride photonic circuits, Nat. Commun. **12**, 2236 (2021).

[11] X. Ji, X. Li, Z. Qiu, R. N. Wang, M. Divall, A. Gelash, G. Lihachev, and T. J. Kippenberg, Deterministic soliton microcombs in Cu-free photonic integrated circuits, Nature (London) **646**, 843 (2025).

[12] H.-J. Chen, K. Colburn, P. Liu, H. Yan, H. Hou, J. Ge, J.-Y. Liu, P. Lehan, Q.-X. Ji, Z. Yuan, D. Bouwmeester, C. Holmes, J. Gates, H. Blauvelt, and K. Vahala, Towards fibre-like loss for photonic integration from violet to near-infrared, Nature (London) **649**, 338 (2026).

[13] B. Shen, L. Chang, J. Liu, H. Wang, Q.-F. Yang, C. Xiang, R. N. Wang, J. He, T. Liu, W. Xie, J. Guo, D. Kinghorn, L. Wu, Q.-X. Ji, T. J. Kippenberg, K. Vahala, and J. E. Bowers, Integrated turnkey soliton microcombs, Nature (London) **582**, 365 (2020).

[14] C. Xiang, J. Liu, J. Guo, L. Chang, R. N. Wang, W. Weng, J. Peters, W. Xie, Z. Zhang, J. Riemensberger, J. Selvidge, T. J. Kippenberg, and J. E. Bowers, Laser soliton microcombs heterogeneously integrated on silicon, Science **373**, 99 (2021).

[15] G. Lihachev, W. Weng, J. Liu, L. Chang, J. Guo, J. He, R. N. Wang, M. H. Anderson, Y. Liu, J. E. Bowers, and T. J. Kippenberg, Platicon microcomb generation using laser self-injection locking, Nat. Commun. **13**, 1771 (2022).

[16] A. S. Raja, A. S. Voloshin, H. Guo, S. E. Agafonova, J. Liu, A. S. Gorodnitskiy, M. Karpov, N. G. Pavlov, E. Lucas, R. R. Galiev, A. E. Shitikov, J. D. Jost, M. L. Gorodetsky, and T. J. Kippenberg, Electrically pumped photonic integrated soliton microcomb, Nat. Commun. **10**, 680 (2019).

[17] A. S. Voloshin, N. M. Kondratiev, G. V. Lihachev, J. Liu, V. E. Lobanov, N. Y. Dmitriev, W. Weng, T. J. Kippenberg, and I. A. Bilenko, Dynamics of soliton self-injection locking in optical microresonators, Nat. Commun. **12**, 235 (2021).

[18] H. Wang, B. Shen, Y. Yu, Z. Yuan, C. Bao, W. Jin, L. Chang, M. A. Leal, A. Feshali, M. Paniccia, J. E. Bowers, and K. Vahala, Self-regulating soliton switching waves in microresonators, Phys. Rev. A **106**, 053508 (2022).

[19] S. Deshmukh, T. M. Schneider, and A. Tikan, Bifurcation structure of soliton self-injection locking in microresonators, Opt. Lett. **51**, 4817 (2026).

[20] L. A. Lugiato and R. Lefever, Spatial dissipative structures in passive optical systems, Phys. Rev. Lett. **58**, 2209 (1987).

[21] M. Haelterman, S. Trillo, and S. Wabnitz, Dissipative modulation instability in a nonlinear dispersive ring cavity, Opt. Commun. **91**, 401 (1992).

[22] N. M. Kondratiev, V. E. Lobanov, A. V. Cherenkov, A. S. Voloshin, N. G. Pavlov, S. Koptyaev, and M. L. Gorodetsky, Self-injection locking of a laser diode to a high-Q WGM microresonator, Opt. Express **25**, 28167 (2017).

[23] J. Gärtner, P. Trocha, R. Mandel, C. Koos, T. Jahnke, and W. Reichel, Bandwidth and conversion efficiency analysis of dissipative Kerr soliton frequency combs based on bifurcation theory, Phys. Rev. A **100**, 033819 (2019).

[24] P. Parra-Rivas, D. Gomila, L. Gelens, and E. Knobloch, Bifurcation structure of periodic patterns in the Lugiato-Lefever equation with anomalous dispersion, Phys. Rev. E **98**, 042212 (2018).

[25] P. Parra-Rivas, D. Gomila, L. Gelens, and E. Knobloch, Bifurcation structure of localized states in the Lugiato-Lefever equation with anomalous dispersion, Phys. Rev. E **97**, 042204 (2018).

[26] L. Bengel, Stability of solitary wave solutions in the Lugiato–Lefever equation, Z. Angew. Math. Phys. **75**, 130 (2024).

[27] L. Bengel and B. de Rijk, Existence and stability of soliton-based frequency combs in the Lugiato–Lefever equation, Phys. D **483**, 134922 (2025).

[28] C. Godey, I. V. Balakireva, A. Coillet, and Y. K. Chembo, Stability analysis of the spatiotemporal Lugiato-Lefever model for Kerr optical frequency combs in the anomalous and normal dispersion regimes, Phys. Rev. A **89**, 063814 (2014).

[29] M. Stanislavova and A. G. Stefanov, Asymptotic stability for spectrally stable Lugiato-Lefever solitons in periodic waveguides, J. Math. Phys. **59**, 101502 (2018).

[30] A. E. Ulanov, T. Wildi, N. G. Pavlov, J. D. Jost, M. Karpov, and T. Herr, Synthetic reflection self-injection-locked microcombs, Nat. Photon. **18**, 294 (2024).

[31] L. Bengel, Codes to "Enhanced soliton stability in bi-directionally coupled laser-microresonator systems", Radar, Karlsruhe Institute of Technology, 2026, 10.35097/ccmqsda449ghm9k6.

[32] H. Uecker, D. Wetzel, and J. D. M. Rademacher, pde2path - A Matlab package for continuation and bifurcation in 2D elliptic systems, Numer. Math. Theory Methods Appl. **7**, 58 (2014).

[33] H. Kielhöfer, *Bifurcation Theory*, 2nd ed., Applied Mathematical Sciences (Springer, New York, 2012), Vol. 156, pp. viii+398.